

## Anomalous diffusion of energetic particles: connecting experiment and simulations

This article has been downloaded from IOPscience. Please scroll down to see the full text article.

2012 Nucl. Fusion 52 103018

(<http://iopscience.iop.org/0029-5515/52/10/103018>)

View [the table of contents for this issue](#), or go to the [journal homepage](#) for more

Download details:

IP Address: 130.183.100.98

The article was downloaded on 07/08/2013 at 13:16

Please note that [terms and conditions apply](#).

# Anomalous diffusion of energetic particles: connecting experiment and simulations

M.J. Pueschel<sup>1,2,3</sup>, F. Jenko<sup>1</sup>, M. Schneller<sup>1</sup>, T. Hauff<sup>1</sup>, S. Günter<sup>1</sup>  
and G. Tardini<sup>1</sup>

<sup>1</sup> Max-Planck-Institut für Plasmaphysik, EURATOM Association, D-85748 Garching, Germany

<sup>2</sup> Max-Planck-Institut für Sonnensystemforschung, D-37191 Katlenburg-Lindau, Germany

<sup>3</sup> Physics Department, University of Wisconsin-Madison, Madison, WI 53706, USA

E-mail: [mjp@physics.wisc.edu](mailto:mjp@physics.wisc.edu)

Received 19 May 2012, accepted for publication 22 August 2012

Published 13 September 2012

Online at [stacks.iop.org/NF/52/103018](http://stacks.iop.org/NF/52/103018)

## Abstract

Recent experimental and theoretical studies highlight the need to predict the turbulence-induced radial diffusion of energetic particles quantitatively in present-day and future fusion devices. Gyrokinetic simulations with passive fast ion species in realistic tokamak equilibria are used to investigate the influence of the particle energy on diffusion due to electrostatic and electromagnetic turbulence. To facilitate more straightforward comparisons between theory and experiments, scaling relations are derived that allow for writing the relevant diffusivities as functions of experimentally readily accessible quantities. In this context, an improved method for estimating the magnetic fluctuation level is described.

(Some figures may appear in colour only in the online journal)

## 1. Introduction

Energetic particles in magnetic confinement fusion experiments may be produced, e.g., through fusion reactions, neutral beam injection (NBI) and—in the case of runaway electrons which, however, require a relativistic treatment—disruptions. Since such fast particle species can contain a lot of energy, it is desirable to both understand and in most cases minimize the impact of the diffusive processes that cause these particles to be transported towards the plasma edge. Another aspect emerging as a consequence of the presence of fast particles in the plasma is the possible excitation of Alfvén eigenmodes—while such modes constitute an important field of study (see, e.g., [1, 2] for recent publications), the focus in this work shall lie exclusively on the impact of background (micro-)turbulence on fast ions.

Recent experimental studies of fast particle dynamics in NBI-heated plasmas have illustrated the need for a deeper understanding of turbulent diffusion of fast particles under realistic conditions (see, e.g. [3]). The authors of [4, 5], analysing a DIII-D discharge conclude that their results imply a relevant level of microturbulence-induced fast particle transport at moderately suprathreshold energies. More experimental studies at different fusion devices are currently

underway, further exploring this effect, as well as possible links to an observed reduction in the current drive efficiency due to NBI in certain situations.

Turbulent transport of energetic particles has also received a significant amount of attention recently from theorists. In addition to studies regarding alpha particle transport in ITER [6–8], the turbulent diffusion of beam ions has become a renewed focus area. Theories describing the energy dependence of the energetic particle diffusivities, based on orbit decorrelation [9, 10] and orbit averaging [11, 12] have been put forth. The results obtained through these approaches differ only slightly in their energy dependence for trapped particles. Studies of the impact of fast ion diffusion on experimental scenarios have also been undertaken [13, 14], where non-negligible transport was found to impact both fusion alphas and NBI ions.

This work aims to compare numerical results from fast particle studies in gyrokinetic turbulence with analytical models for cases with realistic tokamak equilibria. However, since theoretical predictions tend to include parameters which are difficult to measure in fusion experiments, such as correlation lengths, in a second step all such quantities are replaced by more convenient observables.

After some details on the analytical theory and the numerical setup used in this work, fast particle simulations

in realistic ASDEX Upgrade and DIII-D geometries will be presented in section 4, with particular emphasis on the impact of the particle energy, the pitch angle and the geometry on the fast particle diffusivity. In this context, the applicability of the relevant expressions given in section 2 will be demonstrated in their respective limits. For easier comparisons of experimental results, a database of various gyrokinetic turbulence simulations will be used in section 5 to reduce the parameter dependences in the aforementioned expressions to experimentally more easily accessible quantities.

## 2. Theoretical background

In the context of diffusion of fast particles due to background microturbulent fields, [9, 15] distinguish electrostatic and magnetic turbulence; by considering (ballistic) decorrelation from the background turbulence through drift motion and using a basic diffusion model, they arrive at expressions for the diffusivities. These expressions are valid in certain limits of the (cosine of the) pitch angle  $\eta$  (technically: the pitch), where  $\eta = v_{\parallel}/v$  and  $v_{\parallel}$  and  $v$  are the parallel and total velocity, respectively. In the following, the letters p and t indicate passing ( $\eta \rightarrow 1$ ) and trapped ( $\eta \rightarrow 0$ ) particles. Normalized to  $c_s \rho_s^2 / R_0$ , the fast ion diffusivities read [15]

$$D_{\text{fi,p}}^{\text{es}}(E) \approx \frac{v_E^2 \lambda_V}{3\eta^2} \left( \frac{E}{T_e} \right)^{-1}, \quad (1)$$

$$D_{\text{fi,t}}^{\text{es}}(E) \approx \frac{1.73 v_E^2 \lambda_c \lambda_V \epsilon_t^{1/2}}{12\pi^{1/2} \eta (1 - \eta^2)} \left( \frac{E}{T_e} \right)^{-3/2} \quad (2)$$

for the electrostatic contributions, and

$$D_{\text{fi,p}}^{\text{em}}(E) \approx \left( \frac{B_r}{B_0} \right)^2 \frac{\lambda_B}{3}, \quad (3)$$

$$D_{\text{fi,t}}^{\text{em}}(E) \approx \frac{1.73 (B_r/B_0)^2 \lambda_B^2 \epsilon_t^{1/2} \eta}{12\pi^{1/2} (1 - \eta^2)} \left( \frac{E}{T_e} \right)^{-1/2} \quad (4)$$

for the electromagnetic counterparts, where  $\rho_s = c_s / \Omega_i$  denotes the ion sound gyroradius,  $c_s = (T_e / m_i)^{1/2}$  is the ion sound speed,  $\Omega_i$  is the ion Larmor frequency,  $T_e$  is the electron temperature,  $m_i$  is the ion mass and  $R_0$  is the major radius of the flux surface under investigation. Moreover,  $v_E$  is the  $E \times B$  velocity, normalized to  $c_s \rho_s / R_0$ ; while the radial magnetic field can be expressed as  $B_r = \mathcal{C}(\beta / \beta_{\text{crit}}) B_0 \rho_s / R_0$  relative to the background magnetic field  $B_0$ , with a scalar factor  $\mathcal{C}$  (see [16, 17]); this approach will be improved upon in section 5) and the normalized electron plasma pressure  $\beta = 8\pi n_e T_e / B_0^2$ —here,  $n_e$  is the electron density—relative to its kinetic ballooning mode threshold  $\beta_{\text{crit}}$ . The correlation lengths  $\lambda_V$ ,  $\lambda_c$  and  $\lambda_B$  are associated with the electric field, electric potential and magnetic potential, respectively, and are normalized to  $\rho_s$ . Finally,  $E$  is the kinetic particle energy, while  $\epsilon_t = r_0 / R_0$  is the inverse aspect ratio of the flux surface at radial position  $r_0$ .

Expressions (1) and (3) for passing particles were obtained in the limit of small gyroradii. This approximation, however, breaks down when  $E/T_e$  becomes sufficiently large compared

with  $1 - \eta^2$ . In that case, the corresponding equations for large gyroradii have to be used [15],

$$D_{\text{fi,p-FLR}}^{\text{es}}(E) \approx \frac{1.73 v_E^2 \lambda_c \lambda_V}{12\pi^{1/2} \eta^2 (1 - \eta^2)^{1/2}} \left( \frac{E}{T_e} \right)^{-3/2} \quad (5)$$

for the electrostatic and

$$D_{\text{fi,p-FLR}}^{\text{em}}(E) \approx \frac{1.73 (B_r/B_0)^2 \lambda_B^2}{12\pi^{1/2} (1 - \eta^2)^{1/2}} \left( \frac{E}{T_e} \right)^{-1/2} \quad (6)$$

for the electromagnetic case, where FLR stands for finite Larmor radius. Note that the energy dependences have now steepened to  $E^{-3/2}$  and  $E^{-1/2}$ , respectively, compared with fully passing particles, and that these modified cases are applicable for a significant energy range in the vicinity of  $\eta \sim 0.9$ —as  $\eta$  gets very close to 1, the original prescriptions become valid again. The trapped particle limits already incorporate large-gyroradius effects, and therefore no such modification is necessary. Other than these limits, the following assumptions were made to obtain the above equations: the turbulence is isotropic in the directions perpendicular to the magnetic field, and decorrelation occurs more quickly in those directions than parallel to the field. While the first assumption constitutes a simplification, it can easily be extended to anisotropic cases using the smaller of the perpendicular correlation lengths instead of the isotropic correlation length; the latter assumption is valid in typical fusion experiments, as orbit averaging breaks down, making perpendicular decorrelation much faster than its parallel counterpart [9].

As mentioned before, the energy slope  $E^{-3/2}$  in (2) does not conform with the respective result reported in [12], where the scaling was found to be steeper, with  $E^{-2}$ . It should be noted that this relatively moderate difference can be hard to distinguish in simulations when taking into account any error bars, even when resolving the high- $E$  range more thoroughly, as was carried out in this work.

## 3. Numerical approach

Numerical simulations were performed with the radially local version of the GENE code<sup>4</sup> [18], a nonlinear gyrokinetic Vlasov code that includes fully electromagnetic physics of arbitrary numbers and types of particle species. For a review of gyrokinetics, see [19]. Use was made of a code feature that allows the designation of particle species as *passive*: a passive species evolves according to the Vlasov equation and the electrostatic and electromagnetic fields (where parallel magnetic fluctuations are neglected, an approximation that is valid in the moderate- $\beta$  regime of this work, as long as  $\beta < (T_e/T_{\text{fi}})^{1/2}$ , where  $T_{\text{fi}}$  is the fast ion species temperature), but does not act back on any other species via the field equations. This ansatz does not include the physics of fast particle modes, but instead provides a description of the behaviour of fast tracer particles in the background turbulence created by the thermal ions and electrons—it should be noted that this is in accordance with the interpretations in [4].

Simulations with fast ions involve a particle species with a high bulk temperature  $T_{\text{fi}} \gg T_e$ —the values used in the

<sup>4</sup> <http://gene.rzg.mpg.de>

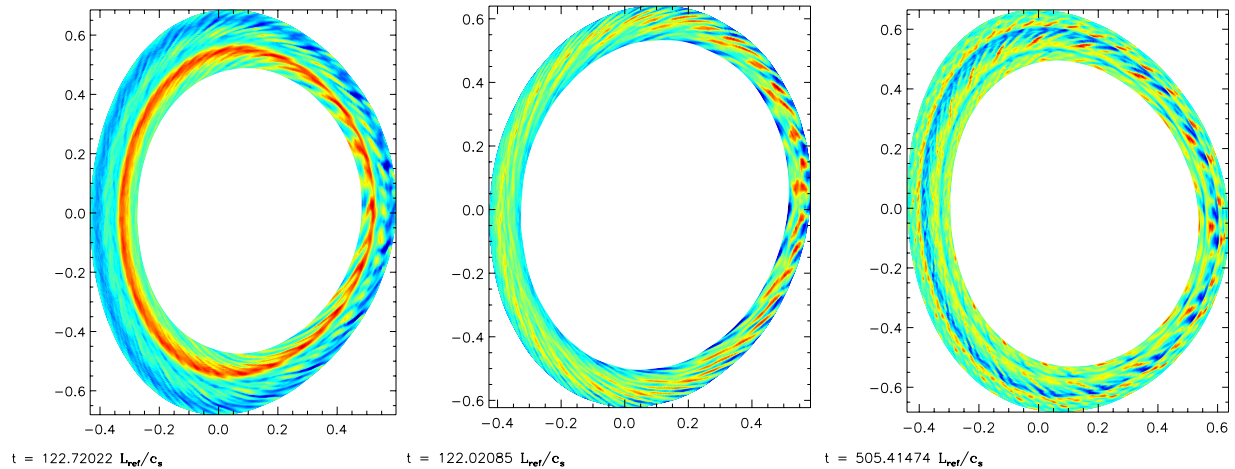


**Figure 1.** Flux surface shapes of ASDEX Upgrade shots #18383 (left) and #18703 (centre), as well as DIII-D shot #134426 (right). The axes correspond to the usual  $(R, Z)$  coordinates, with  $(0, 0)$  lying on the magnetic axis. The turbulent contour data correspond to snapshots of the electrostatic potential during the saturated nonlinear phase. A lower triangularity (shaping) than in the other geometries was used for the centre case; it is shown in this work that—while this has an impact on the background turbulence—the applicability of analytical theory is not influenced.

simulations range from  $T_{fi}/T_e = 50$ – $500$  unless specified otherwise (the precise value determines the available  $E$  range in the plots but does not affect the results at a given value of  $E$ ). Thus, the time step of those simulations is typically determined by the hot fast ion species (generally labelled  $fi$ ), which, apart from the additional numerical effort required to solve the Vlasov equation for said species, significantly increases the overall computational requirements. Like the background species, the equilibrium distribution function  $F_{fi0}$  of the fast ion species is Maxwellian, but  $F_{fi0}$  drops out in the analyses shown in this work.

To resolve the background turbulence, resolutions around  $N_x = 128$ – $192$  were used for the radial direction,  $N_{ky} = 16$ – $24$  for the binormal Fourier space,  $N_z = 16$ – $24$  for the coordinate parallel to the background magnetic field, as well as  $N_{v\parallel} = 48$ – $64$  and  $N_\mu = 16$ – $24$  for the parallel velocity and magnetic moment coordinates, respectively. Compared with the real space resolutions, the velocity space is thus resolved somewhat more finely, which was done in order to improve analyses of the energy dependence of the fast ion particle transport and diffusivity.

The velocity space extends from  $-3$  to  $3$  for  $v_\parallel$  (in units of the thermal velocity  $v_{Tj} = (2T_j/m_j)^{1/2}$  of species  $j$ ) and  $0$  to  $9v_{Tj}^2$  for  $\mu$ . While the grid in  $v_\parallel$  (the parallel velocity coordinate) is equidistant, the  $\mu$  (the magnetic moment coordinate) values are based on either Gauss–Legendre or Gauss–Laguerre quadrature (the choice does not change any of the results of this work) such that, in particular, the range near  $\mu = 0$  is resolved sufficiently well. The fact that the velocity space of a given species is normalized to its thermal velocity ensures that the fast ions can be resolved with the same number of grid points as the background ions and electrons.

In order to be able to define a particle diffusivity, the fast ion species are subjected to a (normalized) density gradient  $\omega_{n,fi}$  that is set to the same value as the background density gradient  $\omega_n$  of the active species and which is later eliminated in the analysis. No temperature gradient  $\omega_{T,fi}$  is used for the fast ion species. In this work, any (density or temperature)

gradient is defined as  $\omega_{n,T} = R_0/L_{n,T}$ , where  $L_{n,T}$  is the (density or temperature) gradient scale length.

The numerical convergence of simulations with only the active species was ensured separately, whereas requirements for the fast particle species were gauged through comparison with (1)–(6) and [9, 20].

In the next section, specific examples of turbulent fields in realistic magnetic geometries are examined.

#### 4. Fast particles in realistic geometries

Simulations were performed in three different realistic geometries: ASDEX Upgrade shots #18383 and #18703, as well as DIII-D discharge #134426—in all cases, the radial position for the (local flux tube) simulations was chosen as  $\rho_{tor} = 0.5$ . The ASDEX Upgrade shots were subjected to off-axis NBI and central electron cyclotron heating; for the DIII-D shot, off-axis NBI was also used. Figure 1 shows the shapes of the flux surfaces for those three geometries. All three experiments were dedicated to the study of fast particles, with AUG #18703 exhibiting a significantly weaker shaping than #18383—for more details on the three discharges, see [3] (ASDEX Upgrade) and [4] (DIII-D). In all three cases, both ion temperature gradient driven and trapped electron mode turbulence were found to play a role, with the latter being more prominent in the DIII-D case due to the larger value of  $\omega_{Te}$ .

It is important to note that gyrokinetic simulations without background  $E \times B$  shear tend to produce higher fluxes than those observed in the experiments. Therefore, separate simulations were performed with reduced gradients (compared with the measured values) to match the experimental fluxes. Table 1 lists the physical parameter choices used in the simulations of this section. Here,  $\hat{s}$  is the magnetic shear and  $q_0$  the safety factor at the position of the radial centre of the simulation box (i.e., at  $r = r_0$ ).

In the following, velocity space data will be shown. Since GENE operates on  $v_\parallel$ – $\mu$  space, whereas the relevant analyses on the experimental side require  $E$ – $\eta$  coordinates, the simulation

**Table 1.** Physical simulation parameters for the three discharges discussed in the text. Numbers in brackets denote reduced values which were used to obtain heat fluxes comparable to the experimental results.

<i>ASDEX Upgrade</i> #18383						
$T_i$	$0.94T_e$	$\epsilon_t$	0.19	$\omega_{Ti}$	4.15	(3.0)
$\beta$	$5.5 \times 10^{-3}$	$q_0$	1.83	$\omega_{Te}$	5.64	(4.0)
$m_e$	$2.7 \times 10^{-4}m_i$	$\hat{s}$	1.16	$\omega_n$	1.59	(1.2)
<i>ASDEX Upgrade</i> #18703						
$T_i$	$1.22T_e$	$\epsilon_t$	0.19	$\omega_{Ti}$	7.3	(4.37)
$\beta$	$3.4 \times 10^{-3}$	$q_0$	1.97	$\omega_{Te}$	8.94	(5.13)
$m_e$	$2.7 \times 10^{-4}m_i$	$\hat{s}$	1.46	$\omega_n$	2.65	(1.59)
<i>DIII-D</i> #134426						
$T_i$	$1.21T_e$	$\epsilon_t$	0.19	$\omega_{Ti}$	5.62	
$\beta$	$8.1 \times 10^{-3}$	$q_0$	1.88	$\omega_{Te}$	4.21	
$m_e$	$2.7 \times 10^{-4}m_i$	$\hat{s}$	0.83	$\omega_n$	0.96	

data are transformed onto the new grid through the relation

$$\mu B_0 = v_{\parallel}^2 \left( \frac{1}{\eta^2} - 1 \right). \quad (7)$$

Note that  $B_0$  is a function of the parallel (poloidal) coordinate, and  $\eta$  is treated as an input parameter; for  $v_{\parallel}$ , all available values on the simulation grid are used, resulting in  $\mu$  values for which the simulation data are obtained through linear interpolation between  $\mu$  grid points, or linear extrapolation where necessary. A variety of alternative interpolation methods was tested, including quadratic and spline interpolation, or specifying a particular  $E(\eta, v_{\parallel})$  grid as an input parameter. Differences due to different interpolation schemes, however, were observed only in the very-high- $E$  regime where statistics can be poor (as very few particles of the fast ion species have the required  $v_{\parallel} \sim v_{\parallel, \max}$ ). Additionally, at the largest  $|v_{\parallel}|$ , the velocity space boundary can have a non-negligible impact. For the purpose of the analyses of this work, no sensitivity with regard to the interpolation method was found except at the  $E_{\max}$  boundary of velocity space, which was therefore excluded from the plots.

The GENE data used here are the particle transport  $\Gamma$  (normalized to  $c_s \rho_s^2 n_0 / R_0^2$ , with the background density  $n_0$ ). It is time averaged and then divided by  $\omega_{n, \text{fi}}$  (in the absence of an  $\omega_{T, \text{fi}}$ ) and a Maxwellian distribution for the fast ions  $F_{\text{fi}0} = F_{\text{fi}0}(\tau, v_{\parallel}, \mu)$  of temperature  $T_{\text{fi}}$  to arrive at the diffusivity

$$D_{\text{fi}}(v_{\parallel}, \mu) = - \frac{\Gamma(v_{\parallel}, \mu)}{\omega_n F_0}. \quad (8)$$

This definition is equivalent to the one used in [14]. It is important to point out that due to the division by  $F_0$ , the region of statistics- and boundary-afflicted energies can be slightly larger than one might anticipate from standard analyses of gyrokinetic simulations, and special caution is required when analysing corresponding data. After the transformation to  $E$ - $\eta$  coordinates, the parallel coordinate is averaged over.

The analyses of this work can be understood as an improved method to the one used in [9]; in particular, they clearly demonstrate the existence of an intermediate- $\eta$  regime where finite Larmor radius effects are important to the dynamics of passing particles, as described by (5) and (6).

Before showing realistic geometry results, data for typical benchmark parameter (Cyclone base case [21]) simulations

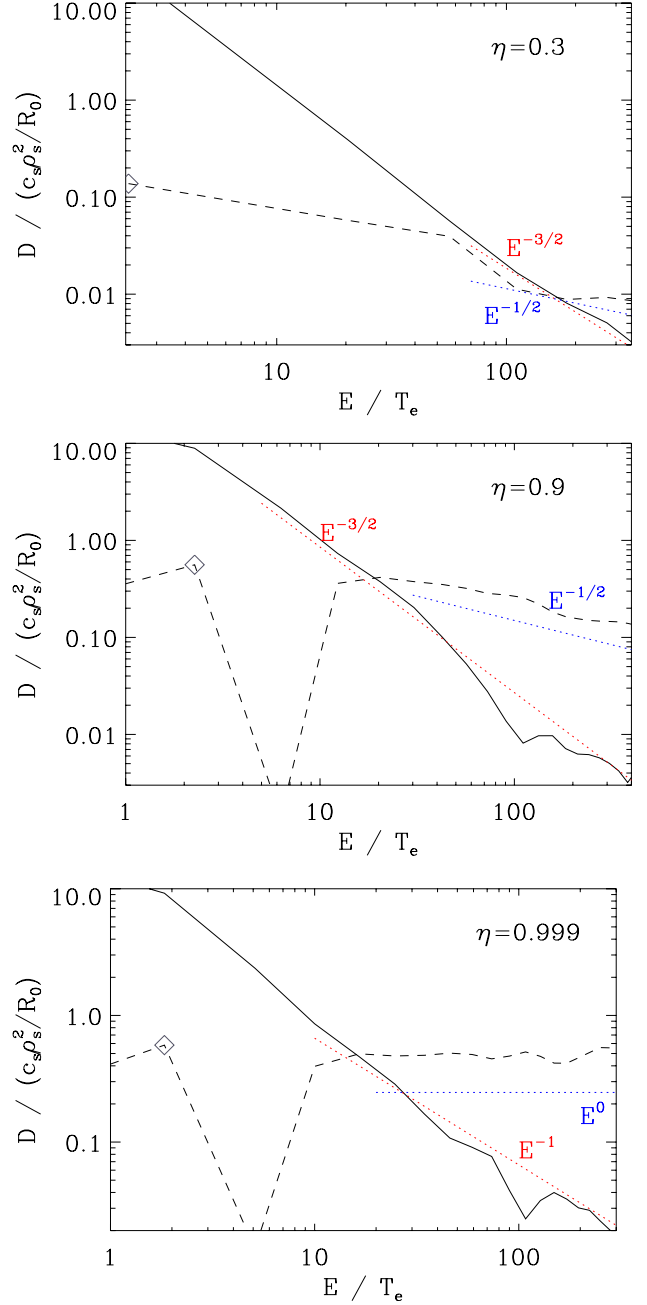


**Figure 2.** Fast particle diffusivities for Cyclone base case parameters ( $\beta = 0.006$ ) in  $\hat{s}$ - $\alpha$  geometry as a function of the particle energy, for pitch angles  $\eta = 0.3$  (top: trapped particle limit),  $0.9$  (middle: passing particle limit for large  $\rho$ ) and  $0.999$  (bottom: fully passing particle limit). The solid line corresponds to the electrostatic, the dashed one to the electromagnetic component. The (labelled) dotted lines illustrate the slopes as predicted by analytic theory (see the text): the red lines of  $D_{\text{fi}} \propto E^{-3/2}$  and  $D_{\text{fi}} \propto E^{-1}$  apply to the electrostatic components, whereas the blue lines of  $D_{\text{fi}} \propto E^{-1/2}$  and  $D_{\text{fi}} \propto E^0$  apply to the electromagnetic components. These lines match the simulation data only in the moderate-to-high- $E$  range, as at lower energies  $E \lesssim 10T_e$ , resonances with the active species are observed. Grey diamonds indicate negative values.

in idealized  $\hat{s}$ - $\alpha$  geometry at  $\beta = 0.006$  can be found in figure 2 (see [16] for more details on physical and numerical properties of these simulations). The physical parameters are identical to those analysed in [9]. Qualitatively, the features

in these plots are the same as in the other cases in this section: at lower energies, typically around  $E \sim 1\text{--}10T_e$ , the fast particle species show a resonance with the active species; beyond that point, the curves follow the analytical predictions in the three regimes of trapped ( $\eta = 0.3$ ), large- $\rho$  passing ( $\eta = 0.9$ ) and fully passing particles ( $\eta = 0.999$ ) rather well, with small deviations arising due to finite statistics and resolutions. Although the value of  $\eta = 0.3$  could be seen as a fairly large pitch angle, considering it is representing the  $\eta \rightarrow 0$  limit, the plots demonstrate the applicability of the trapped particle limit. This is important to keep in mind when analysing experimental data with typical values near  $\eta \sim 0.7$  which can be understood as the boundary of applicability of the trapped and passing regimes; since the slopes for the trapped and large- $\rho$  passing cases are identical, however, they should cover the entire NBI-accessible  $\eta$  range of any experiment.

Note that the absolute values of the analytical curves shown in figure 2, as well as in all other plots in this section, were obtained through the method detailed in section 5, rather than through direct evaluation of the corresponding equations. Also note that the ranges of the abscissas vary from plot to plot, as the coordinate transformation yields different values of  $E$  for given  $\eta$  and  $T_{\text{fi}}$ .

Moving on from idealized  $\hat{s}\text{--}\alpha$  to realistic geometries, it is important to ensure the applicability of the analytical theory in such cases. Figures 3 and 4 show results for ASDEX Upgrade shots #18383 and #18703, respectively, at the nominal gradients. Clearly, all three limits are described well by the theory, suggesting that shaping (triangularity) has little impact on the fast particles other than through its effect on quantities like  $v_E$  and  $B_r$  or the correlation lengths, which is already captured in the equations.

As can be seen in figure 5, the theoretical slopes are similarly applicable for the  $\eta = 0.3$  and  $\eta = 0.9$  cases for DIII-D discharge #134426. The fully passing limit also has the slopes following the analytical predictions of  $E^{-1}$  (electrostatic) and  $E^0$  (electromagnetic) very well; in the electrostatic case, however, the analytical prediction level is too low by a factor of  $\sim 4$ . This may be either a statistical outlier or a consequence of the way the correlation lengths are defined, an issue also discussed in section 5.

The reduced gradient cases mentioned above and in table 1 produce no different picture: figure 6 exemplarily shows a plot for  $\eta = 0.9$  in the #18383 case where the gradients have been lowered; very similar results are obtained for the other ASDEX Upgrade shot, as well as for the other pitch angles. No qualitative difference is found when comparing these results with the nominal gradient simulations. The quantitative changes are a result of the modified background turbulence.

The focus is thus now shifted towards a lower energy range,  $E \sim 10T_e$ , where the theoretical slopes are no longer applicable, but which is of relevance to present-day devices.

Unfortunately, analyses have yielded no simple yet universal description of this energy range—too much depends on the properties of the active species turbulence. In general, one can fit the electrostatic component at energies  $E < 10T_e$  reasonably well with the expression

$$D_{\text{fi}} = D_{10} \left( \frac{E}{T_e} \right)^{-\epsilon \log(E/T_e)}. \quad (9)$$

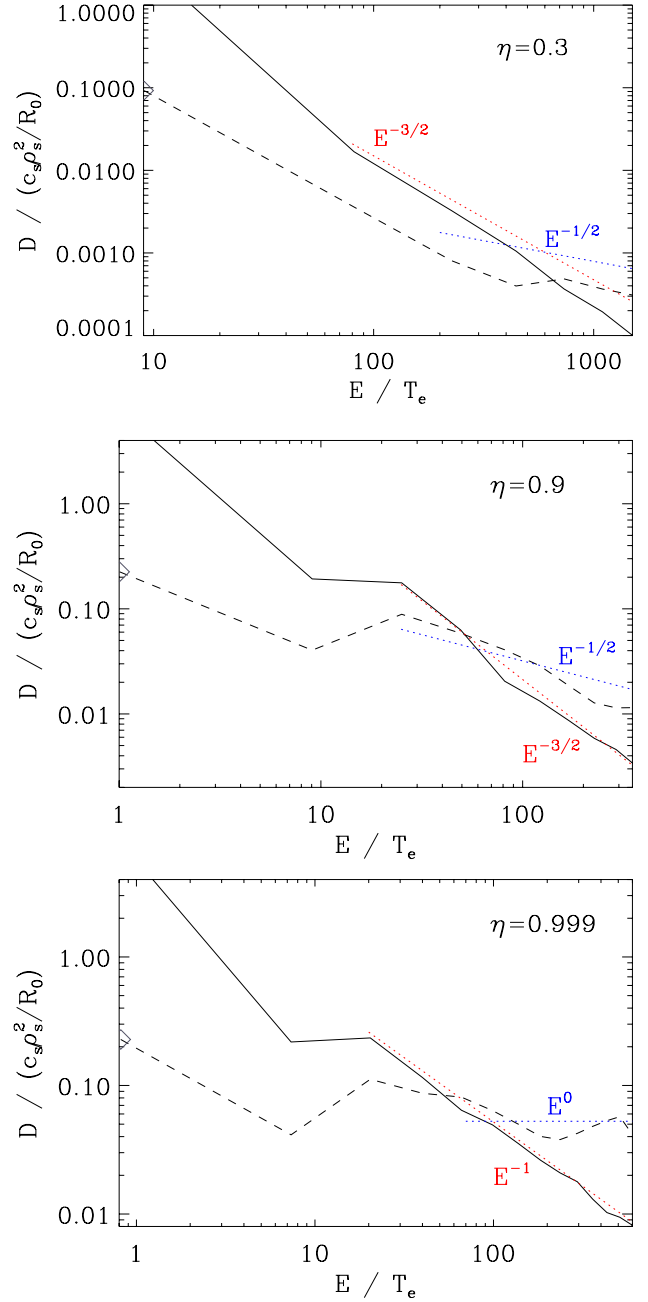


**Figure 3.** Fast particle diffusivities for ASDEX Upgrade shot #18383 as a function of the particle energy, for pitch angles  $\eta = 0.3$  (top: trapped particle limit),  $0.9$  (middle: passing particle limit for large  $\rho$ ) and  $0.999$  (bottom: fully passing particle limit). The solid line corresponds to the electrostatic, the dashed one to the electromagnetic component. For the meaning of the dotted lines and grey diamonds, see the caption of figure 2.

Here,  $D_{10}$  is  $D_{\text{fi}}(E = 10T_e)$  calculated according to the corresponding prescription used throughout this work.  $\epsilon$  is a free parameter, typically  $\sim 1.5\text{--}2$ , but no single choice applies to all cases investigated here. Figure 7 shows one example: ASDEX Upgrade #18383 with  $\eta = 0.9$ , where  $\epsilon = 1.5$  fits the numerical data well in the  $E \sim 1\text{--}10T_e$  regime.

In all the above examples, the magnetic component of  $D_{\text{fi}}$  abruptly changes sign (while roughly preserving its amplitude) near  $E_{\text{fi}} \sim 10T_e$ . This behaviour is the consequence of a particle pinch in the active species,  $\Gamma_{e,i}^{\text{em}} < 0$ , which

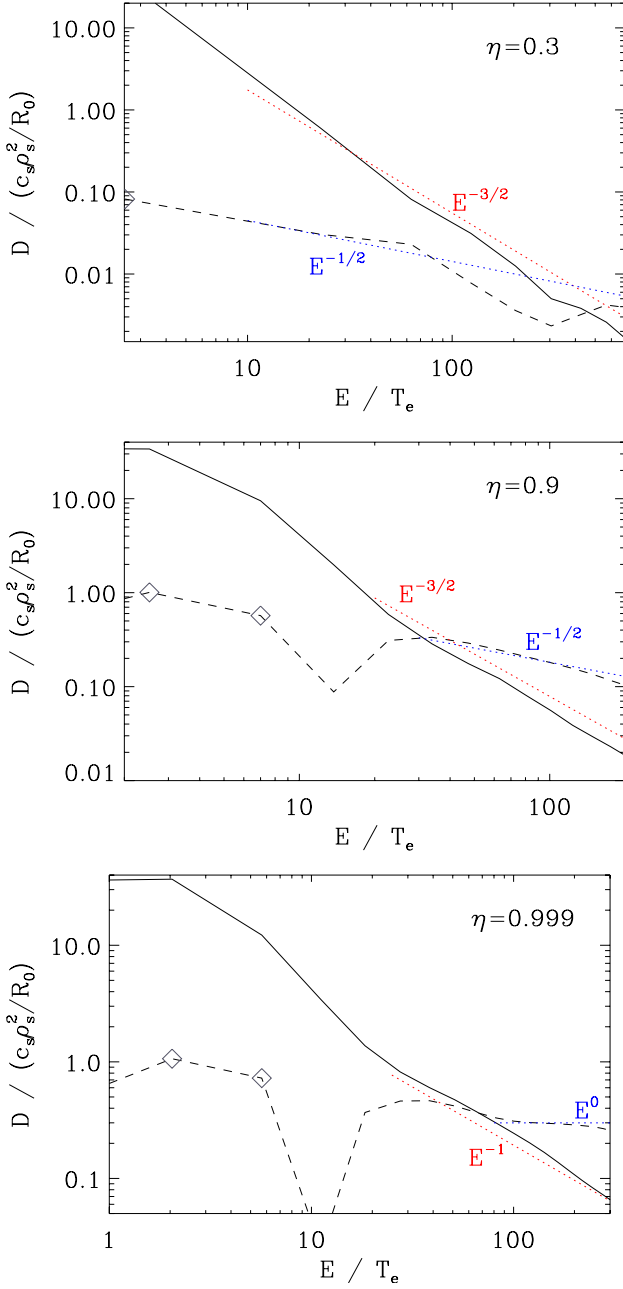


**Figure 4.** Fast particle diffusivities for ASDEX Upgrade shot #18703 as a function of the particle energy, for pitch angles  $\eta = 0.3$  (top: trapped particle limit), 0.9 (middle: passing particle limit for large  $\rho$ ) and 0.999 (bottom: fully passing particle limit). The solid line corresponds to the electrostatic, the dashed one to the electromagnetic component. For the meaning of the dotted lines and grey diamonds, see the caption of figure 2.

is a common feature of gyrokinetic simulations at finite  $\beta$ . In high- $\beta$  scenarios, a similar sign reversal [22] may occur, possibly as a result of the presence of a subdominant microtearing mode [23, 24]. Such inward transport effects could, under the right circumstances, significantly influence the fast particle behaviour in the  $E \gtrsim T_e$  range.

Thus, the full energy range for fast particles cannot in its entirety be characterized without performing direct numerical simulations, as the background species start to have a significant impact on the fast particle behaviour.

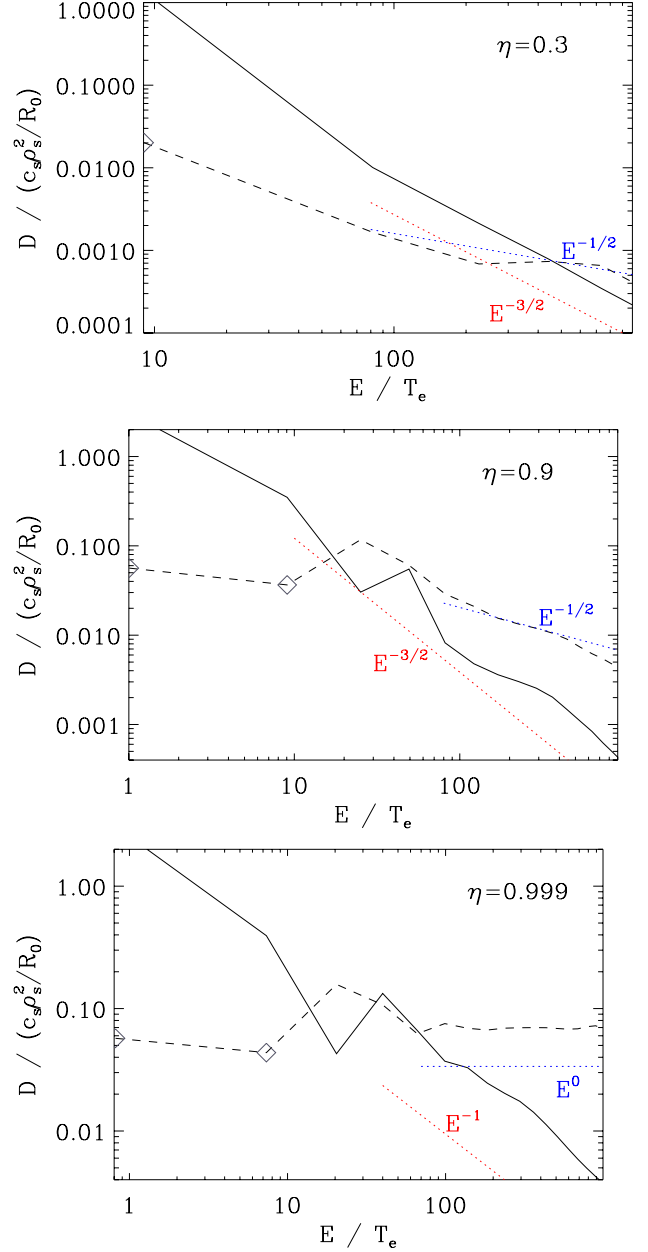


**Figure 5.** Fast particle diffusivities for DIII-D shot #134426 as a function of the particle energy, for pitch angles  $\eta = 0.3$  (top: trapped particle limit), 0.9 (middle: passing particle limit for large  $\rho$ ) and 0.999 (bottom: fully passing particle limit). The solid line corresponds to the electrostatic, the dashed one to the electromagnetic component. For the meaning of the dotted lines and grey diamonds, see the caption of figure 2.

Only at energies around  $E_{fi} \sim 10T_{fi}$  do (1)–(6) begin to become predictive of fast ion diffusion. Coincidentally, the magnetic component  $D_{fi}^{em}$  starts to become comparable to the electrostatic component  $D_{fi}^{es}$  at a similar energy for typical  $\beta$  values. Therefore, when applying the aforementioned equations, or their energy scalings, one automatically should take the magnetic contribution into account.

Next, steps are taken to simplify the use of said equations for comparisons with experimental data by replacing quantities like all  $\lambda$  in the analytical expressions with more common observables.

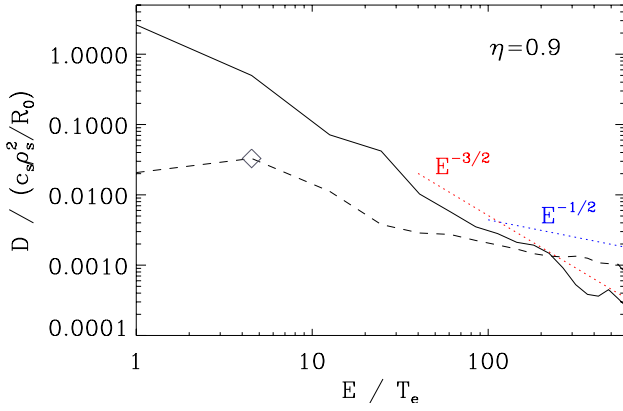


**Figure 6.** Fast particle diffusivities for ASDEX Upgrade shot #18383 at reduced background gradients, as a function of the particle energy, for pitch angle  $\eta = 0.9$  (passing particle limit for large  $\rho$ ). The solid line corresponds to the electrostatic, the dashed one to the electromagnetic component. For the meaning of the dotted lines and grey diamonds, see the caption of figure 2.

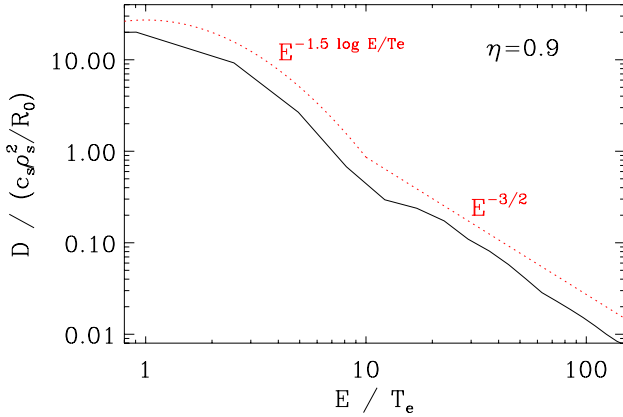


**Figure 7.** Fast particle diffusivities for ASDEX Upgrade shot #18383, as a function of the particle energy, for pitch angle  $\eta = 0.9$  (passing particle limit for large  $\rho$ ). Here a fast ion species with a very moderate  $T_{fi} = 20T_e$  was chosen in order to resolve the low- $E$  range more finely. Shown here is only the electrostatic component. Above  $E = 10T_e$ , the dotted line follows the usual analytical slope; the low- $E$  fit is prescribed by (9) with  $\epsilon = 1.5$ .

## 5. Reduction to accessible variables

It is desirable to attempt validation not only of the energy dependence experimentally—which, if measurements are available for only very few energies, can be difficult—but also of the magnitude of the diffusivity as predicted by (1)–(6). A direct evaluation of this set of equations requires knowledge of quantities like  $v_E$  or correlation lengths which are difficult or even impossible to measure directly and can thus introduce large errors.

In this section, all ‘inaccessible’ parameters in those equations are substituted by quantities which can be measured easily and without excessive error bars: the thermal diffusivity  $\chi_{\text{eff}} = \chi_i + \chi_e = \chi_{\text{es}} + \chi_{\text{em}}$ , normalized to  $c_s \rho_s^2 / R_0$ , (identical to the normalization of  $D_{fi}$ ), and the electron  $\beta$ , or more specifically:  $\beta / \beta_{\text{crit}}$ . Since the following substitutions imply significant simplifications when using the resulting prescriptions, those prescriptions are meant to serve as a tool for estimation rather than an exact analysis method.

For most cases,  $\chi_{\text{em}}$  will be significantly smaller than  $\chi_{\text{es}}$ ; thus, while the separation of the electrostatic and electromagnetic contributions is not possible experimentally,  $\chi_{\text{eff}}$  still serves as a good indicator for the electrostatic  $v_E$ . As the radial diffusivity is of interest in this work, one may set  $v_E \equiv v_{Er}$ . On the electromagnetic side,  $\beta$  constitutes a good measure for the magnetic fluctuation strength  $B_r$  (compare, e.g., [17, 20]). Since  $\eta$  and  $\epsilon_t$  are known quantities in fusion experiments, that leaves only the correlation lengths which tend not to change very dramatically throughout the simulations in the database. As mentioned before, the analytical work in [9] is based on isotropic turbulent fields (in the perpendicular directions  $x$  and  $y$ )—since the fastest decorrelation process is of interest, the prescription  $\lambda_{\text{corr}} = \min(\lambda_x, \lambda_y)$  is used for the correlation lengths. The magnetic correlation length  $\lambda_B$  is simply that of the magnetic potential  $A_{\parallel}$ , and thus  $\lambda_B \equiv \lambda_{A_{\parallel}}$ . Note that throughout this work, numerically obtained  $\lambda_{\text{corr}}$  are measured at the outboard midplane (corresponding to the centre of the flux tube along the parallel coordinate), where the turbulence is strongest, making it the most relevant region when studying decorrelation. In addition, the correlation lengths are found not to change much in the vicinity of the outboard midplane.

To facilitate the aforementioned variable replacements, a database of gyrokinetic turbulence simulations was created. These simulations include various nonlinear, radially local gyrokinetic studies performed with the GENE code. In addition to all the parameter sets from section 4, parameters from  $\hat{s}$ - $\alpha$  geometry  $\beta$  scans described in [16, 17], as well as from background pressure gradient studies of those cases, from ASDEX Upgrade discharges #24681, #24682 and #26459, and from JET discharge #70084 were used. For the electromagnetic case, microtearing simulations from [25] (with negligible electrostatic transport) are included in the magnetic plots. From all these simulations, the relevant quantities (e.g., correlation lengths, heat diffusivities) were extracted by analysing the simulation data over the whole nonlinear saturation phase.

As a useful by-product of the database, a possible artefact of computing the correlation lengths is eliminated through statistics: In some cases, mostly for the electrostatic  $\lambda_c$ , the auto-correlation function decays quickly with the  $y$  coordinate at first (in particular, more quickly than with  $x$ ), but then levels off suddenly near a value of  $e^{-1} \approx 0.37$  which is used in the standard definition of  $\lambda_y$ . Depending on whether this threshold is reached or not,  $\lambda_{\text{corr}}$  will in such cases by definition be equal to  $\lambda_y$  or  $\lambda_x$ . By substituting the database results for the explicit correlation lengths, such problematic threshold effects are removed.

Figure 8 shows the electrostatic results for both trapped and passing particles, clearly establishing linear relationships between the total heat diffusivity and the quantities involved in (1) and (2), excluding the energy and pitch angle dependences. The somewhat larger spread of the data points for the trapped particle case can be attributed to the fact that more quantities enter into (2). Overall, however,  $\chi_{\text{eff}}$  serves as an excellent indicator of electrostatic fast particle diffusion. The proportionality constants of the fits are  $\bar{\sigma}_{\text{es,p}} = 2.63$  and  $\bar{\sigma}_{\text{es,t}} = 25.9$ , defined via  $\bar{\sigma}_{\text{es,p}} \chi_{\text{eff}} = v_E^2 \lambda_V$ , and analogously for the trapped particle limit.

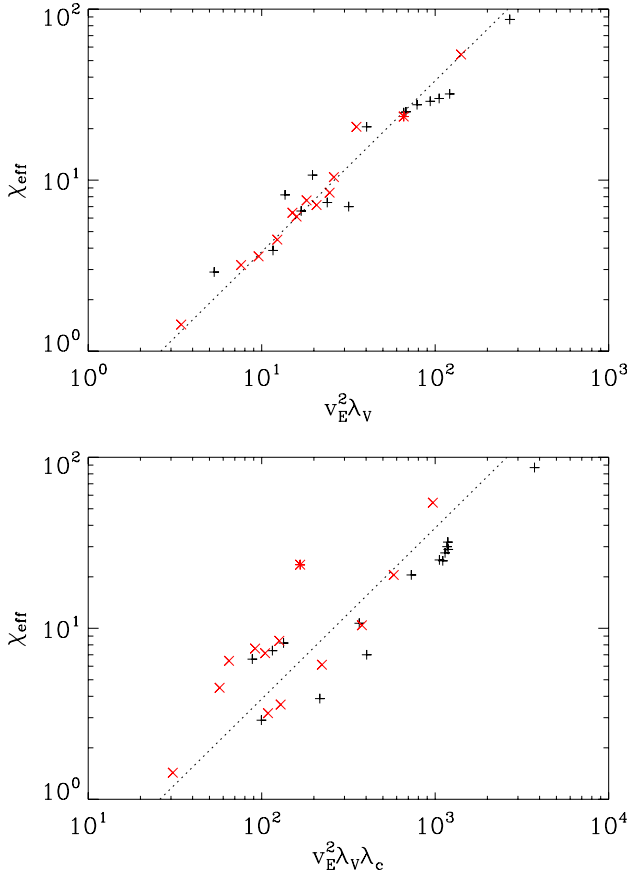


**Figure 8.** Electrostatic results for the simulation database in the passing (above: compare (1)) and trapped (below: compare (2)) limit. Black t's symbolize simulations in  $\hat{s}$ - $\alpha$  geometry, red crosses simulations in realistic geometries of ASDEX Upgrade, DIII-D and JET discharges; the red star denotes an ASDEX Upgrade simulation near the edge. The dotted fit curve is a straight line fixed to the origin, illustrating directly proportional relations for both cases.

The only prominent deviation (in the trapped particle case) from the fit, marked by a red star, stems from a simulation from near the tokamak edge; since that same simulation produces outliers in the electromagnetic fits (both passing and trapped limits), it may be conjectured that additional effects come into play when one approaches the edge region—further study beyond the scope of this work would be necessary in order to obtain a better understanding of such cases.

The electromagnetic equivalent turns out to require additional modifications, as is illustrated in figure 9 for fully passing particles, corresponding to (3). The first plot is obtained using  $\beta_{\text{crit}} = \beta_{\text{crit}}^{\text{MHD}}$  (see [16]) which, while often a good estimate for  $\hat{s}$ - $\alpha$  geometry, can yield poor results for shaped flux surfaces. It is worth noting that the deviation of the actual  $\beta_{\text{crit}}$  from the MHD value (as defined in [16]) can be interpreted as a measure of the strength of the shaping. Using instead the value of  $\beta_{\text{crit}}$  as measured in linear simulations at representative  $k_y$ , the fit quality is enhanced significantly, see the second plot, where additionally, a correction factor  $\mathcal{C}$  is applied that depends solely on the turbulence type. In [17], the respective values are reported as  $\mathcal{C}_{\text{ITG}} = 0.76$ ,  $\mathcal{C}_{\text{TEM}} = 0.16$  and  $\mathcal{C}_{\text{ITG-TEM}} = 0.4$  for cases where both ITG (ion temperature gradient) and TEM (trapped electron mode) characteristics are present in the turbulence. From the simulation database,

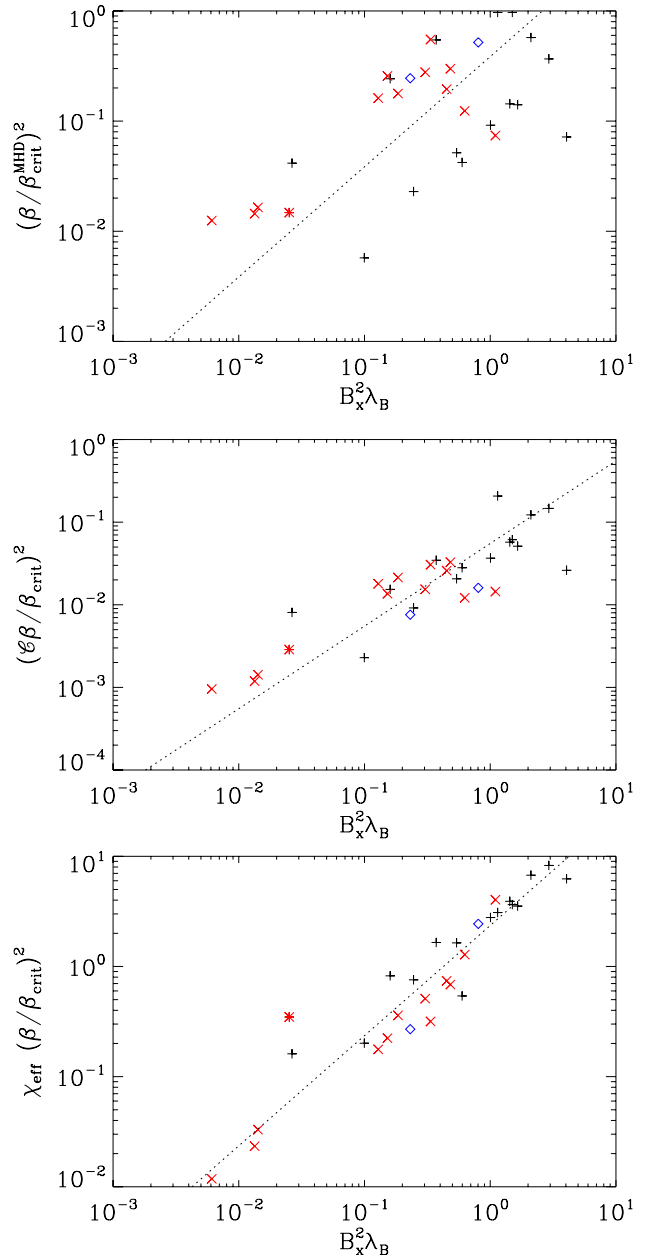


**Figure 9.** Electromagnetic results for the simulation database in the passing limit (compare (3)). The same nomenclature as in figure 8 is used, with the additional blue diamonds corresponding to microtearing simulations. From top to bottom, the plots show data with  $\beta_{\text{crit}}$  obtained through the standard  $\alpha^{\text{MHD}} = 0.6\hat{s}$  estimate;  $\beta_{\text{crit}}$  from linear gyrokinetic simulations (for the non- $\hat{s}$ - $\alpha$  cases) modified via the turbulence type coefficient  $\mathcal{C}$ ; and without  $\mathcal{C}$  but including a factor of  $\chi_{\text{eff}}$ . The latter constitutes the final result.

however, statistically more significant data can be extracted by fitting the different turbulence type groups separately. This procedure yields slightly modified coefficients  $\mathcal{C}_{\text{ITG}} = 0.60$ ,  $\mathcal{C}_{\text{TEM}} = 0.37$ ,  $\mathcal{C}_{\text{ITG-TEM}} = 0.44$ , as well as  $\mathcal{C}_{\text{MT}} = 0.18$  for microtearing cases—note that for the data points for the TEM case [17],  $\beta_{\text{crit}} = \beta_{\text{crit}}(k_y = 0.3)$  instead of  $\beta_{\text{crit}} = \min_{k_y} \beta_{\text{crit}}(k_y)$  was used, where  $k_y = 0.3$  roughly corresponds to the spectral transport peak.

Alternatively, however, one may avoid requiring knowledge of the turbulence type by considering the fact that

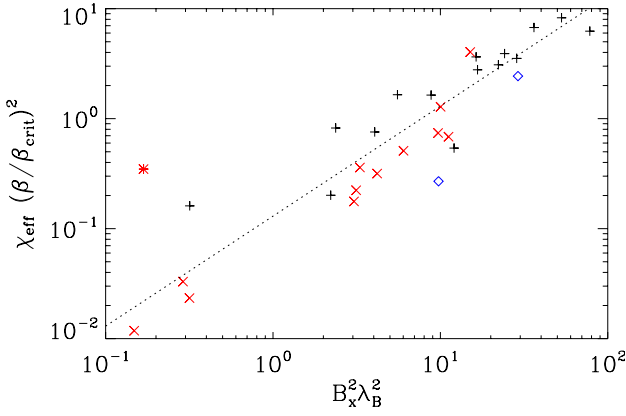


**Figure 10.** Electromagnetic results for the simulation database in the trapped limit (compare (4)). The same nomenclature as in figure 8 is used, with the additional blue diamonds corresponding to microtearing simulations.

stronger (electrostatic) turbulence amplitudes tend to create stronger magnetic fluctuations. Therefore, in the lowermost plot in figure 9, a factor of  $\chi_{\text{eff}}$  was multiplied onto the  $(\beta/\beta_{\text{crit}})^2$  term, but leaving out the previous factor of  $C$ . Thus, the scatter of the data points is reduced even further, underlining the universality of the procedure. Now the same method is applied to the trapped particle case, with the final result shown in figure 10, corresponding to (4). The relevant slopes for the electromagnetic cases are  $\bar{\sigma}_{\text{em,p}} = 0.425$  and  $\bar{\sigma}_{\text{em,t}} = 7.70$  for the passing and trapped limits, respectively, defined in the same way as their electrostatic counterparts.

To arrive at the final form of the equations, two additional modifications are made to the original slopes  $\bar{\sigma}$ : first, all numerical prefactors are absorbed by defining  $\bar{\sigma}_p = \bar{\sigma}_p/3$  and  $\bar{\sigma}_t = 1.73 \bar{\sigma}_t/(12\pi^{1/2})$ , identically for both the electrostatic and electromagnetic quantities. Then, the resulting equations are fitted to the numerical data for all four geometries in section 4, and—in order to account for deviations arising from, e.g., the definitions of the correlation lengths—an offset factor (identical for all geometries) is applied to match the curves:  $\sigma_p = \bar{\sigma}_p/3$ ,  $\sigma_{p\text{-FLR}} = \bar{\sigma}_{p\text{-FLR}}/5$  and  $\sigma_t = \bar{\sigma}_t/4$ . The final values for the coefficients thus become (including the large- $\rho$  limits)

$$\sigma_{\text{es,p}} = 0.292, \quad \sigma_{\text{es,p-FLR}} = 0.422, \quad \sigma_{\text{es,t}} = 0.527, \quad (10)$$

$$\sigma_{\text{em,p}} = 0.047, \quad \sigma_{\text{em,p-FLR}} = 0.125, \quad \sigma_{\text{em,t}} = 0.157. \quad (11)$$

These values can now be used to reduce (1) and (2) to

$$D_{\text{fi,p}}^{\text{es}} \approx \frac{\sigma_{\text{es,p}} \chi_{\text{eff}}}{\eta^2} \left( \frac{E}{T_e} \right)^{-1} \quad (12)$$

and

$$D_{\text{fi,t}}^{\text{es}} \approx \frac{\sigma_{\text{es,t}} \chi_{\text{eff}} \epsilon_t^{1/2}}{\eta(1-\eta^2)} \left( \frac{E}{T_e} \right)^{-3/2}, \quad (13)$$

respectively. The electromagnetic equivalents, (3) and (4), become

$$D_{\text{fi,p}}^{\text{em}} \approx \sigma_{\text{em,p}} \chi_{\text{eff}} \left( \frac{\beta}{\beta_{\text{crit}}} \right)^2 \quad (14)$$

and

$$D_{\text{fi,t}}^{\text{em}} \approx \frac{\sigma_{\text{em,t}} \chi_{\text{eff}} (\beta/\beta_{\text{crit}})^2 \epsilon_t^{1/2} \eta}{1-\eta^2} \left( \frac{E}{T_e} \right)^{-1/2}, \quad (15)$$

while (5) and (6) can be treated equivalently to the trapped cases:

$$D_{\text{fi,p-FLR}}^{\text{es}} \approx \frac{\sigma_{\text{es,p-FLR}} \chi_{\text{eff}}}{\eta^2 (1-\eta^2)^{1/2}} \left( \frac{E}{T_e} \right)^{-3/2} \quad (16)$$

and

$$D_{\text{fi,p-FLR}}^{\text{em}} \approx \frac{\sigma_{\text{em,p-FLR}} \chi_{\text{eff}} (\beta/\beta_{\text{crit}})^2}{(1-\eta^2)^{1/2}} \left( \frac{E}{T_e} \right)^{-1/2}. \quad (17)$$

These six expressions constitute the central result of this work, and can be used to express  $D_{\text{fi}}$  in all relevant limits as a function of the pitch angle  $\eta$ , the fast ion energy  $E$ , the effective heat diffusivity  $\chi_{\text{eff}}$ , the normalized plasma pressure  $\beta$  and the inverse aspect ratio  $\epsilon_t$ , all of which are known or can be measured directly and with good confidence in fusion experiments.

While the results of this section may benefit, e.g., from including simulations exhibiting more and also more exotic geometries, or a more thoroughly evaluated  $\beta_{\text{crit}}$  based on a two-dimensional  $\beta$ - $k_y$  scan, they provide good prescriptions for estimating the impact of the turbulent fields on the diffusion of fast particles, while simultaneously offering new insights into some fundamental properties of turbulence.

## 6. Conclusions

In this paper, the turbulence-induced radial transport of energetic ions in tokamak plasmas was investigated, taking into account realistic magnetic geometries. Building on previous analytical and numerical work (for simplified geometries), the main focus was to derive expressions which allow for a relatively straightforward application to actual experiments.

It was found that—independently of the flux surface shape—at sufficiently large fast ion energies  $E \gtrsim 10T_e$ , the analytical energy dependencies as derived in [9, 15] are reproduced correctly, whereas at lower energies, resonances with the active species become important and lead to non-universal behaviour. Thus, if the injection energy of NBI ions is sufficiently large relative to the background temperature, the model provides good quantitative predictions of turbulent diffusivities. In the case of fusion  $\alpha$  particles, the energy scale separation is always sufficiently large.

Since the analytical expressions contain physical quantities (like the radial correlation lengths of the fluctuating electromagnetic fields) which are very hard to obtain experimentally, a database of gyrokinetic simulations was composed through which it was demonstrated that these quantities can be replaced by more accessible ones with reasonable accuracy. Such substitutions make direct comparisons with the experiment much easier and, in particular, allow for straightforward assessment of the relative impact of the electromagnetic to the electrostatic contribution (i.e., determination where  $D_{\text{fi}}^{\text{es}}$  and  $D_{\text{fi}}^{\text{em}}$  intersect; see also [26]). It was shown that the heat diffusivity  $\chi_{\text{eff}}$  of the active species can be used to replace both the electrostatic  $v_E$  and the electromagnetic  $B_r$ , along with the relevant correlation lengths. In the latter case, an additional factor of  $(\beta/\beta_{\text{crit}})^2$  was included to gauge the magnetic fluctuation level. The database results, and in particular the values for the coefficients  $\sigma$  as reported in section 5, clearly illustrate that for sufficiently

large  $\beta$ , magnetic fast particle diffusivity can become dominant even at moderate  $E$ .

As a byproduct of this study, it was shown that the (radial) magnetic fluctuation level need not depend on the turbulence type and may be expressed as

$$B_x \equiv B_r \propto \chi_{\text{eff}}^{1/2} \frac{\beta}{\beta_{\text{crit}}}. \quad (18)$$

A very similar prescription should apply to  $B_y$  (see [17]). Regarding future work, in addition to expanding the parameter ranges of the simulation database, it may be useful to study the impact of equilibrium  $E \times B$  shear. The effect of microtearing modes may require more investigation, in particular in the context of realistic discharge modelling. Also, the last stage of the process detailed in section 5—the final fit to the fast particle data—would benefit from the inclusion of more simulations with passive fast ion species. Radially global simulations are not envisioned to be necessary, however: it is expected that the picture does not change much for ITER-like NBI parameters.

## Acknowledgments

Part of this work was supported by the Max Planck Society through the Interinstitutional Research Initiative ‘Turbulent transport and ion heating, reconnection, and electron acceleration in solar and fusion plasmas’, project MIF-IF-A-AERO8047. The authors would like to thank J. Hobirk, P.W. Terry and T. Kurki-Suonio for valuable discussions, as well as D. Told and H. Doerk for making their simulation data available for analysis.

## References

- [1] Heidbrink W.W. 2008 *Phys. Plasmas* **15** 055501
- [2] Breizman B.N. and Sharapov S.E. 2011 *Plasma Phys. Control. Fusion* **53** 054001
- [3] Günter S. *et al* and the ASDEX Upgrade Team 2007 *Nucl. Fusion* **47** 920
- [4] Heidbrink W.W., Murakami M., Park J.M., Petty C.C., Van Zeeland M.A., Yu J.H. and McKee G.R. 2009 *Plasma Phys. Control. Fusion* **51** 125001
- [5] Heidbrink W.W., Park J.M., Murakami M., Petty C.C., Holcomb C. and Van Zeeland M.A. 2009 *Phys. Rev. Lett.* **103** 175001
- [6] Estrada-Mila C., Candy J. and Waltz R.E. 2006 *Phys. Plasmas* **13** 112303
- [7] Angioni C. and Peeters A.G. 2008 *Phys. Plasmas* **15** 052307
- [8] Kurki-Suonio T., Asunta O., Hirvijoki E., Koskela T., Snicker A., Hauff T., Jenko F., Poli E. and Sipilä S. 2011 *Nucl. Fusion* **51** 083041
- [9] Hauff T., Pueschel M.J., Dannert T. and Jenko F. 2009 *Phys. Rev. Lett.* **102** 075004
- [10] Dannert T., Günter S., Hauff T., Jenko F., Lapillonne X. and Lauber P. 2008 *Phys. Plasmas* **15** 062508
- [11] Zhang W., Lin Z. and Chen L. 2008 *Phys. Rev. Lett.* **101** 095001
- [12] Zhang W., Decyk V., Holod I., Xiao Y., Lin Z. and Chen L. 2010 *Phys. Plasmas* **17** 055902
- [13] Albergante M., Graves J.P., Fasoli A., Jenko F. and Dannert T. 2009 *Phys. Plasmas* **16** 112301
- [14] Albergante M., Graves J.P., Fasoli A., Jucker M., Lapillonne X. and Cooper W.A. 2011 *Plasma Phys. Control. Fusion* **53** 054002
- [15] Hauff T. 2009 Transport of energetic particles in turbulent plasmas *PhD Thesis* University of Ulm
- [16] Pueschel M.J., Kammerer M. and Jenko F. 2008 *Phys. Plasmas* **15** 102310
- [17] Pueschel M.J. and Jenko F. 2010 *Phys. Plasmas* **17** 062307
- [18] Jenko F., Dorland W., Kotschenreuther M. and Rogers B.N. 2000 *Phys. Plasmas* **7** 1904
- [19] Brizard A.J. and Hahm T.S. 2007 *Rev. Mod. Phys.* **79** 421
- [20] Pueschel M.J. 2009 Electromagnetic effects in gyrokinetic simulations of plasma turbulence *PhD Thesis* University of Münster
- [21] Dimits A.M. *et al* 2000 *Phys. Plasmas* **7** 969
- [22] Hein T., Angioni C., Fable E. and Candy J. 2010 *Phys. Plasmas* **17** 102309
- [23] Hatch D.R., Terry P.W., Jenko F., Merz F., Pueschel M.J., Nevins W.M. and Wang E. 2011 *Phys. Plasmas* **18** 055706
- [24] Hatch D.R., Pueschel M.J., Nevins W.M., Jenko F., Terry P.W. and Doerk H. 2012 *Phys. Rev. Lett.* **108** 235002
- [25] Doerk H., Jenko F., Pueschel M.J. and Hatch D.R. 2011 *Phys. Rev. Lett.* **106** 155003
- [26] Pueschel M.J. 2011 Transport of fast particles in turbulent fields *AIP Conf. Proc.* submitted